Journal of Innovative Optical Health Sciences
Vol. 12, No. 2 (2019) 1950010 (12 pages)
© The Author(s)
DOI: 10.1142/S179354581950010X

J. Innov. Opt. Health Sci. 2019.12. Downloaded from www.worldscientific.com
by HUAZHONG UNIVERSITY OF SCIENCE AND TECHNOLOGY on 04/14/19. Re-use and distribution is strictly not permitted, except for Open Access articles.

Combined spatial frequency spectroscopy analysis with visible resonance Raman for optical biopsy of human brain metastases of lung cancers

Yan Zhou*, Cheng-Hui Liu†, Yang Pu†, Binlin Wu‡, Thien An Nguyen†, Gangge Cheng*, Lixin Zhou§, Ke Zhu¶, Jun Chen‖, Qingbo Li** and Robert R. Alfano†,††

*The Air Force Medical Center, PLA, No. 30
Fuchenglu, Haidian District, Beijing 100142, P. R. China

†Department of Physics
The City College of the City, University of New York
Institute of Ultrafast Spectroscopy and Lasers
NY 10031, USA

‡Physics Department and CSCU Center for Nanotechnology
Southern Connecticut State University, 501 Crescent Street
New Haven, CT 06515, USA

§Beijing Cancer Hospital, No. 52, Fuchenglu
Haidian District, Beijing 100142, P. R. China

¶Institute of Physics, Chinese Academy of Sciences (CAS)
Beijing 100190, P. R. China

‖Department of Cardiology
Tianjin Medical, University General Hospital
Tianjin 300052, P. R. China

**Beihang University, Xueyuan Road
No. 37, Haidian District, Beijing 100191, P. R. China
††ralfano@ccny.cuny.edu

Received 16 December 2018
Accepted 4 March 2019
Published 22 March 2019

The purpose of this study is to examine optical spatial frequency spectroscopy analysis (SFSA) combined with visible resonance Raman (VRR) spectroscopic method, for the first time, to discriminate human brain metastases of lung cancers adenocarcinoma (ADC) and squamous cell carcinoma (SCC) from normal tissues. A total of 31 label-free micrographic images of three types

††Corresponding author.

This is an Open Access article published by World Scientific Publishing Company. It is distributed under the terms of the Creative Commons Attribution 4.0 (CC-BY) License. Further distribution of this work is permitted, provided the original work is properly cited.

of brain tissues were obtained using a confocal micro-Raman spectroscopic system. VRR spectra of the corresponding samples were synchronously collected using excitation wavelength of 532 nm from the same sites of the tissues. Using SFSA method, the difference in the randomness of spatial frequency structures in the micrograph images was analyzed using Gaussian function fitting. The standard deviations, σ calculated from the spatial frequencies of the micrograph images were then analyzed using support vector machine (SVM) classifier. The key VRR biomolecular fingerprints of carotenoids, tryptophan, amide II, lipids and proteins (methylene/methyl groups) were also analyzed using SVM classifier. All three types of brain tissues were identified with high accuracy in the two approaches with high correlation. The results show that SFSA–VRR can potentially be a dual-modal method to provide new criteria for identifying the three types of human brain tissues, which are on-site, real-time and label-free and may improve the accuracy of brain biopsy.

Keywords: Spatial frequency spectroscopy analysis (SFSA); visible resonance Raman (VRR); human brain; metastatic lung cancer; photomicrograph image; support vector machine (SVM).

J. Innov. Opt. Health Sci. 2019.12. Downloaded from www.worldscientific.com
by HUAZHONG UNIVERSITY OF SCIENCE AND TECHNOLOGY on 04/14/19. Re-use and distribution is strictly not permitted, except for Open Access articles.

1. Introduction

Human brain tumors appear regardless of color and age. Brain tumors may arise from a brain's internal tissue (primary brain and central nerve system (CNS) tumors) or external metastases to the brain (metastatic brain tumors). Nearly 700,000 people in 2018 were living with a primary brain and CNS tumor in the USA.[1]

The primary origin of brain cancer is brain neoplasm cells. The secondary or metastatic brain tumors, which have spread to the brain or cerebellum from another location (organ) in the body, are much more common than primary brain tumors. They are the most common brain tumors in adults. Metastatic brain tumors make up about one-fourth of all cancers that spread through the other organs of body. The cerebellum is the part of the brain that watches over complex muscle movements. About 15% of metastatic brain tumors develop in cerebellum, while about 85% of metastatic lesions are located in the cerebrum. The cancers spread to the brain are commonly from lung, breast, colon, kidney, melanoma, thyroid and uterine. The cancer cells of these organs broke free of primary cancer, travel through blood and spread to the brain and grow into the new tumors. The brain metastases of lung cancer are the most common forms of metastatic brain tumor. In fact, lung cancer staging is often found in brain lesion scan before the primary lesion in lung. Approximately 173,770 cases of lung cancer were diagnosed in the US in 2004 with an estimated 160,440 deaths.[2] Small cell lung cancer (SCLC) accounts for approximately 20% of all cases of lung cancers.[3] It tends to disseminate earlier during its natural history than non-SCLC (NSCLC) and is clinically more aggressive.[4]

The conventional diagnosis of brain lesions is performed using biopsy and histopathology. This gold standard method requires freezing specimen or reagent preparation for the biopsy tissue prior to microscopic analysis. This requires skilled technicians and histopathologic experts to perform the diagnosis as well as considerable time before results become available. The subjective nature of the histological evaluation is associated with considerable intra- and inter-observer variation in grading the biopsy tissues, which strongly depends on the experience of the medical doctors. Magnetic resonance imaging (MRI) provides preoperative information about the localization, size and molecular-level biochemical components of the tumor. However, some information is lost during surgery due to tissue changes, e.g., profile shifts, which is the largest concern of the surgeons. In addition, MRI and computed tomography (CT) are expensive *non situ* detection methods that have several disadvantages, such as time-consuming and inflexible.[5,6] Therefore, it is of importance to develop an objective and noninvasive method that can be used for precancerous diagnosis and can be used during clinical practice of surgery.

Optical spectroscopic techniques (e.g., Raman and fluorescence) have demonstrated their advantages of being real-time, *in situ* and label-free in biomedical applications. Since the first report of optical spectroscopic technology used to differentiate human lesions from normal tissues,[7–9] optical spectroscopic techniques have become a major thrust as a potential noninvasive tool to detect

J. Innov. Opt. Health Sci. 2019.12. Downloaded from www.worldscientific.com
by HUAZHONG UNIVERSITY OF SCIENCE AND TECHNOLOGY on 04/14/19. Re-use and distribution is strictly not permitted, except for Open Access articles.

changes in the state of tissues and obtain molecular information. Among them, Raman spectroscopy has been widely used for diagnostic purpose. Recently, native biomarker using Raman spectroscopy was reported in studies of aggressive brain cancers.[10–16]

A visible resonance Raman (VRR) spectroscopy method, in recent years, was shown to have advantages over the conventional Raman technology due to the following reasons: (1) VRR has some unique features. For instance, more resonance Raman (RR) intrinsic biomarkers were observed that have been generated from multiple vibrational modes of larger biomolecules due to resonance Raman using visible 532 nm excitation which matches many biomolecular electronic transition levels in tissues, cells and organelles. (2) VRR signal intensity may be enhanced 10^2 to 10^3 times while operating *in situ* in a time period of seconds. (3) VRR-enhanced signal from vibrational chemical bonds of molecules can be detected at molecular concentrations less than 1.0 nM and the activity of particular molecular species can be targeted preferentially. VRR provides an effective way to enhance Raman signal from particular chemical bonds associated with key molecules and detect their changes at a molecular level, such as carotenoids, tryptophan, amides, lipids and protein in breast, skin, heart, gynecologic and brain lesions.[14,15,17] These advantages of VRR have led to a rapid progress in its applications in brain and other human cancer diagnosis[14,17–21] that are difficult to achieve by conventional nonresonance Raman method.[22–27]

Recently, another new optical spatial frequency spectroscopy analysis (SFSA) method was introduced based on Fourier spatial frequency spectrum analysis of the underlying structure pattern of tissues. The spatial frequency of the structure has been used to analyze microscopic images of cervical cancer at different grades to obtain the information of the periodic and random structures of the tissues.[28–30] The images of certain types of tissue sample contain intensity patterns of the underlying structures, which can be considered as a composition of different spatial frequencies. Spatial frequency spectral analysis method can be used to convert the spatial structure of recorded optical intensities in the images into spatial frequency spectra, analogous to the Fourier decomposition of color frequency spectra with both being frequency-domain analysis.[31] Most importantly, the result of SFSA is a function of the underlying structure of the tissue and can therefore give a truly objective picture of pathology.

This study focuses on analyzing the micrograph images and VRR spectra to find key markers to differentiate human brain metastasis of lung cancer including adenocarcinoma (ADC) and squamous cell carcinoma (SCC) from normal tissues using dual optical modalities of SFSA–VRR, synchronously, *in situ*, *ex vivo*, in real time. The criteria for identification of the three types of brain tissues will be created using SFSA–VRR method. The SFSA–VRR method may have potential for new applications in neuropathology diagnosis and brain surgery.

2. Materials and Methods

Specimens: Human tissues of brain metastases of lung cancer and normal brain tissues were obtained from the Air Force Medical Center, PLA, Beijing, China. All the specimens of brain metastases of lung cancer tissues were carcinomas. Two major subtypes of brain metastasis from lung cancer were used including ADC and SCC. ADC specimens from five patients and SCC specimens from three patients and one normal brain tissue specimen from a noncancer carrying patient were diagnosed. The histopathology reports of metastatic brain tumor and normal brain tissues based on standard pathology and immunohistochemistry methods were obtained for each specimen. According to the stage classification, all investigated tumors are distant cancer metastases with stage IV (The international standard for classification and nomenclature of histology is the International Classification of Diseases for Oncology-ICD-O-3).[32] The experimental procedures were approved by the committee of the Air Force Medical Center, PLA, Beijing, China.

Micrograph images: 30 micrograph images of metastatic brain tumors and normal tissues (4 from normal tissue, 26 from cancerous tissues) were recorded as bright-field reflectance images with white light illumination. Typical micrograph images are shown in Figs. 1(a)–1(c). All images were taken under identical conditions. The micrograph images were obtained label-free using the confocal Raman microspectroscopic system, i.e., Jobin Yvon confocal micro-Raman spectrometer (JY-HR-800 France) with image resolution 500 μm × 380 μm, and image

J. Innov. Opt. Health Sci. 2019.12. Downloaded from www.worldscientific.com
by HUAZHONG UNIVERSITY OF SCIENCE AND TECHNOLOGY on 04/14/19. Re-use and distribution is strictly not permitted, except for Open Access articles.

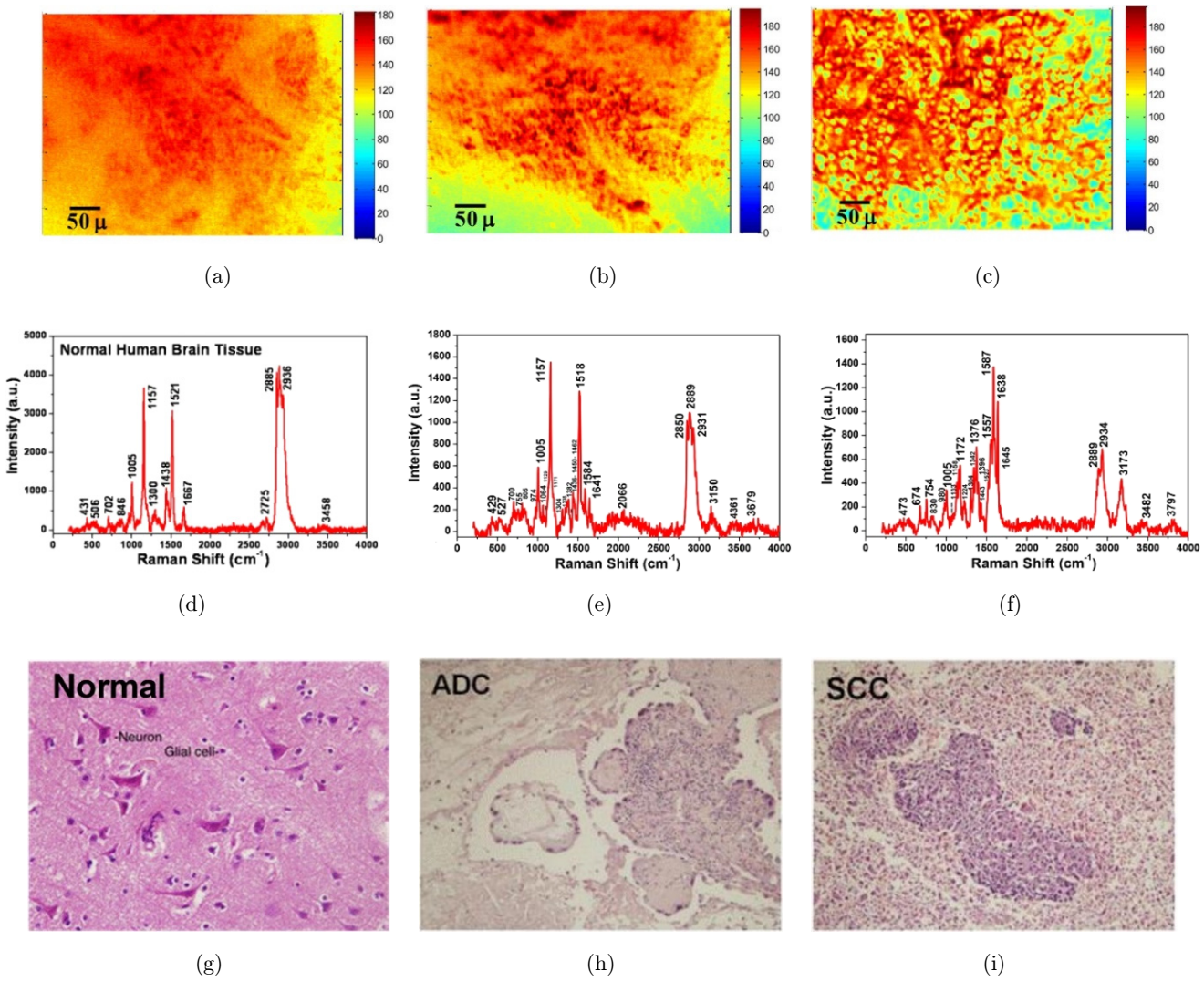

Fig. 1. Three sets of data from brain metastases of lung cancer and normal tissue. Upper row: A set of typical cropped confocal micrograph images using pseudo color of (a) normal brain tissue, (b) brain metastasis from ADC, and (c) brain metastasis from SCC. Middle row: A set of RR spectra of (d) normal brain tissue, (e) brain metastasis from ADC and (f) brain metastasis from SCC. The spectra in (d)–(f) are corresponding to the images in (a)–(c), respectively. Bottom row: H&E-stained images from (g) normal brain tissue, (h) brain metastasis from ADC and (i) brain metastasis from SCC. All the H&E images used 20 × objective and correspond to the images in (a)–(c), respectively.

size 538 pixel × 403 pixels. The micrograph images were recorded before and after VRR data collection in order to confirm the stability and repeatability of the micrograph images.

VRR spectral measurements and Raman instrument: 30 VRR spectra were recorded from the same sites of the specimens where the micrograph images were acquired synchronously. Each brain cancerous tissue was identified by traditional pathology using H&E (hematoxylin and eosin) and immunohistochemical assay as the gold standard (Figs. 1(g)–1(i)). VRR spectra were acquired using confocal micro-HR800 Raman spectrometer with 532 nm excitation wavelength. The detailed description of the instrument was previously reported.[10,18] The excitation light beam was directly shed on the surface of the samples. The spot diameter of the focused laser beam at the sample position is about 1 μm. The laser power at the sample position was 0.9 mW and the typical integration time was 30 s. All spectra were acquired at room temperature. The final spectral resolution was 2 cm^{-1} in the range of interest from 200 to 4000 cm^{-1}. The micrograph images and VRR spectra were then analyzed and compared to the pathology and immunohistochemistry reports.[18]

J. Innov. Opt. Health Sci. 2019.12. Downloaded from www.worldscientific.com
by HUAZHONG UNIVERSITY OF SCIENCE AND TECHNOLOGY on 04/14/19. Re-use and distribution is strictly not permitted, except for Open Access articles.

The basic principle of SFSA: In this paper, the micrographic images (Figs. 1(a)–1(c)) from human brain cancer and normal tissues *ex vivo*, differ from the pathology biopsy images (Figs. 1(g)–1(i)), and were analyzed using SFSA method as described in Refs. 28–30. The current study focuses on human brain metastases of lung cancer. Usually, the intensity distribution of the micrographic image can be expressed as Fourier Transform (FT)[31]:

$$f(x,y) = \sum_{u=0}^{\infty}\sum_{v=0}^{\infty}\left[a_{u,v}\cos\left(\frac{2\pi ux}{L_x}+\frac{2\pi vy}{L_y}\right) + b_{u,v}\sin\left(\frac{2\pi ux}{L_x}+\frac{2\pi vy}{L_y}\right)\right], \quad (1)$$

where u and v are the numbers of cycles of $f(x,y)$ with periods L_x and L_y in the x- and y-directions, respectively. Discrete FT (DFT) is generally used to convert the two-dimensional (2D) spatial intensity distribution function $f(x,y)$ to the 2D spatial spectrum $F(u,v)$ by sampling with a finite extent $N \times N$:

$$F(x,y) = \frac{1}{N}\sum_{x=0}^{N-1}\sum_{y=0}^{N-1} f(x,y)\left[\cos\left(\frac{2\pi(ux+vy)}{N}\right) + j\sin\left(\frac{2\pi(ux+vy)}{N}\right)\right]. \quad (2)$$

The magnitude of spectra, $|F(u,v)|$, is calculated by[15]

$$|F(u,v)| = \sqrt{R^2(u,v)+I^2(u,v)}, \quad (3)$$

where $R(u,v)$ and $I(u,v)$ are the real and imaginary parts of the spatial frequency spectrum, respectively.

Implementation of SFSA: Images of human normal brain tissues and brain tissues of metastases from lung cancers obtained from confocal micrograph were analyzed using Fast FT (FFT) to generate the spatial frequency spectra. Further processing of the spatial frequency spectra allows the extraction of underlying information of the tissue structure.

3. Results and Discussion

Identification of human normal brain tissues and brain tissues of metastases from lung cancer by VRR (1): Three sets of data collected from representative brain metastases of lung cancers (ADC and SCC) and normal tissues are displayed in Fig. 1, including (a) the micrograph images (top row), (b) the VRR spectral data measured synchronously with the micrograph images (middle row) and (c) microscopic images for histopathology diagnosis with H&E stains (bottom row).

VRR spectral fingerprints of carotenoids for ADC and SCC (1): The typical three types of VRR spectra from normal human brain tissues and brain metastases of lung cancers (ADC and SCC) are shown in Figs. 1(d)–1(f), respectively. VRR spectra of key fingerprints from healthy brain tissues in Fig. 1(d) display eight major peaks at 1005, 1157, 1521, 1438, 1667, 2850, 2885, 2932 cm^{-1}, respectively. The relatively sharp and enhanced peaks of 1157 and 1521 cm^{-1} are supposed to arise from carotenoids, low-density lipoprotein (LDL) and high-density lipoprotein (HDL). RR peaks at 1438, 2850 and 2885 cm^{-1} for rich fatty acids are stronger than protein bands at 1005, 1667 and 2934 cm^{-1} in peak intensities. The resonance-enhanced intrinsic molecular fingerprints are supposed to mainly arise from carotenoids with intense RR modes at 1157 cm^{-1} (ν_s(C–C)), 1521 cm^{-1} (ν_s(C=C)) and 1008 cm^{-1} (ρ(C– H_3), ν(C–C)) and major overtone peaks at 2320 and 2667 cm^{-1}. Carotenoids play a significant role in normal brain tissues[33–41] and act against the destructive effect of the free radicals. The specific importance of carotenoids is to serve as a marker substance for the entire anti-oxidative network of human brain tissues.[42,43]

In contrast, in brain cancers, peaks of carotenoids at 1161 and 1521 cm^{-1} are occurring but obviously weaker for ADC and significantly lower or tend to disappear for SCC compared with normal tissue. We proposed that the dependence of the RR spectra of biomarker carotenoids on the tissue types (ADC and SCC) revealed the difference between the types and the status of each type. Our measurements found that these two resonance bands of 1157 (1161) cm^{-1} and 1521 cm^{-1} are active because carotenoids have a pre-resonance absorption band around 480 nm and the excitation wavelength of 532 nm falls in this pre-resonance range. The intensities of RR peaks of 1157 and 1521 cm^{-1} decreased as the type of brain cancer changes from normal to cancerous. This may indicate a progression of different mutation processes. The RR peaks of 1157 and 1521 cm^{-1} diminish sharply for SCC brain tissues (Fig. 1(f)). The suggested reason was that the content of carotenoids decreased, which caused the RR peaks to become too weak to detect or induced a shift in chemical vibration

J. Innov. Opt. Health Sci. 2019.12. Downloaded from www.worldscientific.com
by HUAZHONG UNIVERSITY OF SCIENCE AND TECHNOLOGY on 04/14/19. Re-use and distribution is strictly not permitted, except for Open Access articles.

bands. This may be due to the structural changes within the microenvironment of malignancy. Carotenoids are natural fat-soluble pigments with the reduction of fat. For instance, the peak 1521 cm^{-1} drastically decreases with the decreasing content of saturated fatty acid lipids (1442 and 2850 cm^{-1}). All these observations indicate the existence of a fast activation and deactivation of Raman vibrational modes at 1521 and 1157 cm^{-1} in the types of ADC and SCC brain tissues.[18] RR modes of 1157 and 1521 cm^{-1} could be a significant marker to diagnose metastatic brain cancerous tissues and other cancers.[44,45]

VRR spectral fingerprints of tryptophan for ADC and SCC (2): The key fingerprint of tryptophan molecules with a main vibrational mode at 1587 cm^{-1} (W_{8b}) was observed in the RR spectra.[46–48] It was found that endogenous tryptophan and metabolites contributions were accumulated in brain metastases of lung cancer tissues, and the RR vibrational mode at 1584–1587 cm^{-1} in malignant ADC and SCC (Figs. 1(e) and 1(f)) was enhanced in intensities by resonance. Researchers have reported that heterocyclic amino acid tryptophan is a key factor during the metabolic process in human brain tissues.[49–54] This RR vibrational mode of 1587 cm^{-1} indicates that tryptophan is produced in human metastatic brain tumor of lung cancer and the kynurenine pathway of tryptophan metabolism is involved in brain tumor progression.[46] These observations are in good agreement with changes of tryptophan contents in human brain malignant meningioma and gliomas tissues[10] and skin basal cell carcinoma tissues.[19] The molecular biomarker of tryptophan provides a potential approach to diagnose metastatic brain cancerous tissues and other cancers.

VRR spectral fingerprints of lipid and protein for ADC and SCC (3): The VRR peaks of protein (2934 cm^{-1}) gradually increased in different types of metastatic brain tumors of lung cancer (ADC and SCC) in comparison with normal brain tissues shown in Figs. 1(d)–1(f). The RR mode of 2885 cm^{-1} (2850 cm^{-1}) is correlated with the lipid content and fatty acids of lipids which have intense contributions in normal bran tissues. The increase in the intensity of methyl (–CH3) and decrease in the intensity of methylene (–CH2–) (protein and lipid, both showing symmetric stretch modes of 2934 and 2850 cm^{-1}, 2885 cm^{-1}) were observed in both types of metastatic brain tumor tissues of ADC and SCC. The ratio of RR peaks of protein to lipid ($\mathbf{I}_{2934\,cm^{-1}}/\mathbf{I}_{2885\,cm^{-1}}$) is shown as normal: ADC: SCC to be 0.81: 0.87: 1.31, respectively. The ratio of RR peaks of protein to lipid ($\mathbf{I}_{2934\,cm^{-1}}/\mathbf{I}_{2851\,cm^{-1}}$) is shown as normal: ADC: SCC to be 0.84: 0.94: 2.80, respectively. The result of these ratios reveals the changes of compositions of the macromolecules (e.g., lipids and proteins) during the evolution of the types of brain metastases of lung cancers of ADC and SCC. The lipid (2850 and 2885 cm^{-1}) content decreased in malignant ACC and SCC sharply (shown in Figs. 1(e) and 1(f)). This result is well consistent with the previous reports of Raman spectra of glioblastoma multiforme (GBM) and basal cell carcinoma *ex vivo*.[10,18,19] The ratios serve as a key approach to predict the metastatic potential of brain cancer using VRR spectroscopy analysis.

VRR spectral fingerprint of amide II for ADC and SCC (4): Another important feature indicated by Figs. 1(d)–1(f) is the increase of the protein line in the amide II active bond at 1548–1554 cm^{-1} in ADC and SCC in comparison with normal brain tissues. Intense resonance enhancement of 1555 cm^{-1} band in SCC cancer and less increase in ADC cancer were observed. It reveals biomarker amide II and is important to differentiate ADC and SCC from normal brain tissues. Amide II is one of the nine amide bands of protein and was also resonance-enhanced in gliomas and meningeal cancers due to 532 nm-excited amide II vibrational mode.[10,17,18] Usually, the amide II band is weak or absent in the non-RR system.

Identification of human normal brain tissues and brain metastases of lung cancer by morphology (5): The images of Figs. 1(a), 1(g), 1(b), 1(h) and 1(c), 1(i) were taken from intracranial brain region of normal tissue and metastatic brain tumor of lung cancers of ADC and SCC, respectively. In the images of the normal brain tissue shown in Figs. 1(a) and 1(g), the main compositions such as proteins, lipids and lipoproteins, which make up neuronal and glial cells, are more ordered in layers and uniform in shape and size while these ordered features differ in cancer tissues. This can be observed in the images of ADC in Figs. 1(b) and 1(h) and SCC in Figs. 1(c) and 1(i), which display a periodic, but random, anti-symmetrical, and disordered structure. These features were also observed in prostate, breast and other types of tumors.[55–57]

The microscopic images with H&E staining used for the gold standard histopathology diagnosis are

J. Innov. Opt. Health Sci. 2019.12. Downloaded from www.worldscientific.com
by HUAZHONG UNIVERSITY OF SCIENCE AND TECHNOLOGY on 04/14/19. Re-use and distribution is strictly not permitted, except for Open Access articles.

shown in Figs. 1(g)–1(i). It indicates that Figs. 1(h) and 1(i) for cancerous tissues lack normal tissue structure as shown in Fig. 1(g), and the brain cancer of ADC shown in Fig. 1(h) demonstrates points of gray–red tissues. Moreover, a few atypical cells can be seen among a large piece of necrotic tissue for SCC in Fig. 1(i), indicating that gray–red precipitate and metastatic-differentiated SCC is associated with necrosis in brain cancer tissues.

Identification of human normal brain tissue and brain metastases from lung cancers by SFSA (6): *The analyses of the spatial frequency distribution by SFSA*: In Fig. 2, the 2D spatial spectra were obtained using DFT in Eq. (2). By sampling with $N = 512$, where N is a finite sampling extent, Figs. 2(a)–2(c) display the typical 2D amplitude spectra of normal, ADC and SCC of brain tissues, respectively. For visualization purpose, the amplitude spectra shown in Fig. 2 are exhibited as logarithms of original amplitudes[28] and linearly mapped in the color range of [0, 255]. One-dimensional (1D) spatial frequency spectra (dot lines) through the peaks of the 2D amplitude spectra and their corresponding fitted Gaussian distributions (solid lines) are shown in Fig. 2 for (d) normal tissue, (e) ADC and (f) SCC.

The dominant amplitude of the spatial frequency spectra is close to the origin ($u = 0$, $v = 0$) and decreases in all directions away from the center.[31] These typical results of spatial frequency distribution clearly show strong signal at low spatial frequencies, but weak signal at high frequencies. These differences are also displayed in the 1D frequency spectra in Figs. 2(d)–2(f) that are generated from data shown in Figs. 2(a)–2(c). The results indicated a difference between the two classes of brain tissues including normal and cancerous tissues (with two subtypes of ADC and SCC). It is shown that higher frequency components are more contributive in brain cancerous tissues than in brain normal tissues. The SFSA results from Fig. 2 are summarized as follows: for the normal tissue, the lower frequency amplitudes mostly dominate over the mid-range and high-frequency range as shown in Fig. 2(a). However, the amplitude of mid-range and high-frequency range can be clearly perceived with the evolution from normal tissue in Fig. 2(a) to ADC in Fig. 2(b) and SCC in Fig. 2(c). These differences

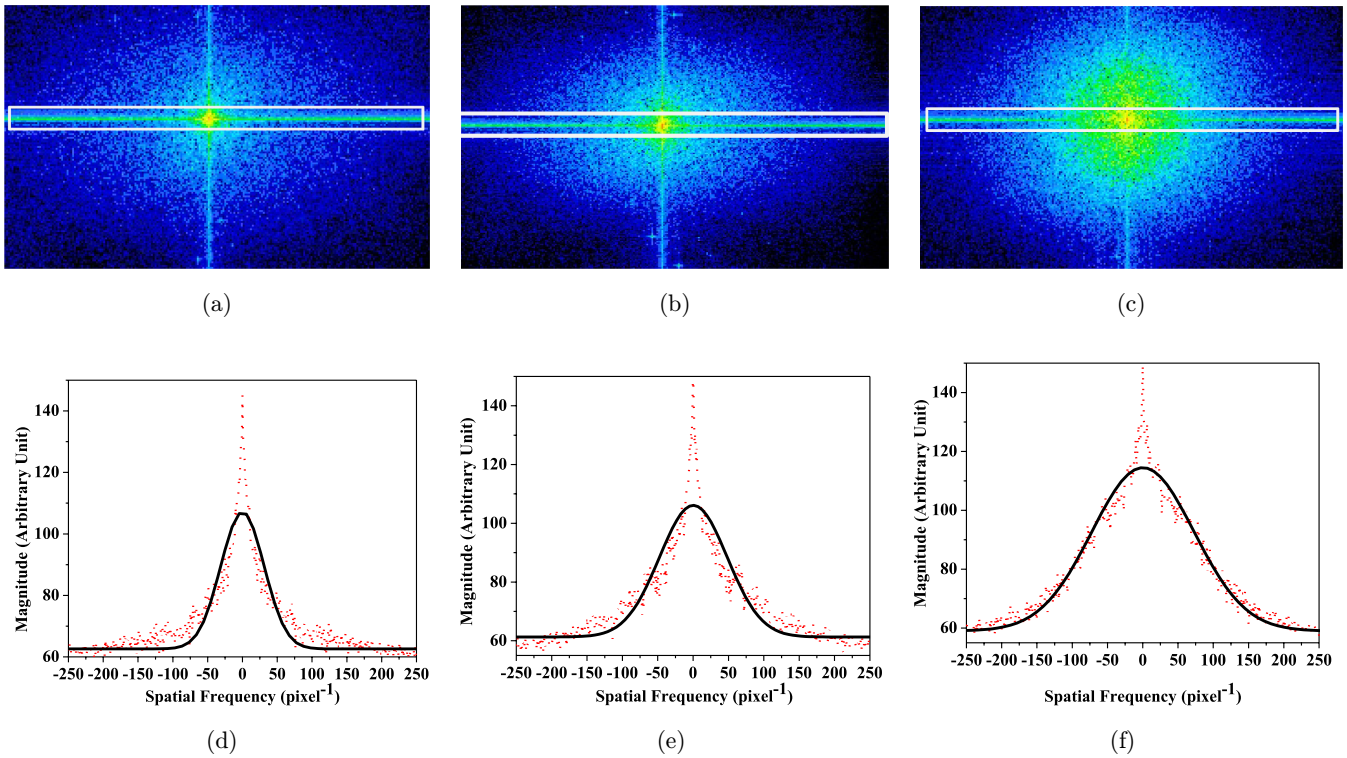

Fig. 2. (a)–(c) are 2D spatial frequency spectra obtained from their corresponding confocal microscope images shown in Figs. 1(a)–1(c), respectively; (b)–(d) are 1D spatial frequency spectra (dot line) along the horizontal direction through the peaks of the 2D spectra in (a)–(c), respectively, along with their corresponding fitted Gaussian distributions (solid line).

J. Innov. Opt. Health Sci. 2019.12. Downloaded from www.worldscientific.com
by HUAZHONG UNIVERSITY OF SCIENCE AND TECHNOLOGY on 04/14/19. Re-use and distribution is strictly not permitted, except for Open Access articles.

among the different types of tissues can be more distinctly seen from their 1D spatial frequency distributions along horizontal direction as shown in Figs. 2(d)–2(f), which are generated by integrating spatial frequency distributions over the vertical direction in the rectangle of solid line in Figs. 2(a)–2(c), respectively. It is shown that spatial frequency spectral profile of the SCC type of brain metastasis of lung cancer is wider than that of normal tissue.

In order to utilize the difference of the width of the spatial frequency spectra to differentiate the types of tissues, the width of the spatial frequency spectra needs to be quantified. The data shown in Figs. 2(d)–2(f) were fitted using Gaussian distribution with zero mean:

$$g(x) = \frac{1}{\sigma\sqrt{2\pi}} \exp\left(-\frac{(x-\mu)^2}{\sigma^2}\right), \qquad (4)$$

where μ is the mean or expectation of the distribution (which is zero in all of our cases), and σ is the standard deviation which is the diversity or "dispersion" of the data away from the mean. A lower σ indicates that the contributing frequencies are close to the mean or zero frequency, whereas higher σ suggests that the data spread over a larger range of frequencies. The fitted curves obtained by a built-in function of Origin 8.5 are shown as solid lines in Figs. 2(d)–2(f).

The differences in σ among different types of tissues were used to evaluate the tissue types. Figure 3(a) shows σ of normal (circle) and cancer (square) tissues, obtained by fitting the experimental data to the Gaussian function in Eq. (4). An increase in the spatial frequency range from normal to cancerous tissues is seen in Fig. 3(a). The expanding spectral range refers to more high-frequency components. This is called "broadening of the signal".[58] The spatial frequency spectra of cancerous tissues are wider when compared with normal tissue. This may provide a diagnostic criterion (σ) for distinguishing brain tumor tissues from normal tissue.

To evaluate the potential use of σ as a criterion, a support vector machine (SVM)[59] is used to analyze the alterations of σ from normal to different types of cancerous tissues. In general, the SVM classifier is determined by a number of "data points" with the most effective discrimination, the support vectors (SVs), which are usually chosen from those at the boundary of the groups of data. In our study for separating normal and cancerous tissues, the SVs are chosen to be σ values between $\sigma^C_{\min} - k$ and $\sigma^N_{\max} + k$, where k is a self-defined threshold value for optimum, and $\sigma^N_{\min}$ and $\sigma^N_{\max}$ are the minimal σ for cancerous tissues and maximal σ for normal tissues, respectively. All the analyses of SVM are performed in Matlab and were presented in detail in our previous study.[60] This standard will be used to classify an unknown data set in the future study when a large number of samples is available.

Classification of metastatic brain tumors from normal brain tissues based on the SFSA–VRR data by SVM classifiers: The SFSA with SVM analysis on micrograph images is well consistent with the VRR with SVM analysis. The results of both methods were compared with gold standard reports.

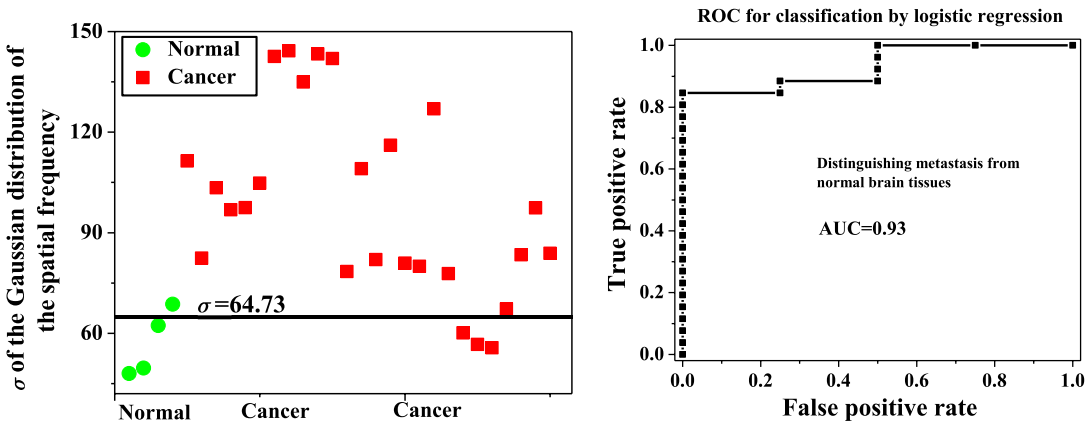

Fig. 3. (a) The σ of the spatial frequency spectra of four normal brain tissues and 26 cancerous brain tissues. The solid line is calculated using SVM to classify the two tissue types. (b) The ROC curve is used to evaluate the performance of the SVM model.

J. Innov. Opt. Health Sci. 2019.12. Downloaded from www.worldscientific.com
by HUAZHONG UNIVERSITY OF SCIENCE AND TECHNOLOGY on 04/14/19. Re-use and distribution is strictly not permitted, except for Open Access articles.

In a diagnostic test, the outcome may be a positive predictive value (disease) or a negative predictive value (healthy), which can be either true or false. The sensitivity and specificity then can be calculated as

$$\text{Sensitivity} = \frac{\#\text{of True Positive}}{\#\text{of True Positive} + \#\text{of False Negative}},$$

$$\text{Specificity} = \frac{\#\text{of True Negative}}{\#\text{of True Negative} + \#\text{of False positive}}.$$

Diagnostic results of SVM classifier based on VRR[18]: The brain metastasis of lung cancer and normal brain tissue specimens were classified based on the VRR spectra using SVM.[10,59,61] The SVM classifier used a Gaussian kernel and yielded diagnostic sensitivity, specificity and accuracy of 100%, 75.0% and 96.7%, respectively.

Diagnostic results of SVM classifier based on SFSA: To test the potential of the diagnosis method using σ, the criterion (threshold) for classifying the positive and negative groups in our study are determined using the SVM on all the tissue samples. It is shown that $\sigma = 64.73$ denoted by the solid line accurately discriminates normal brain tissues from cancerous brain tissues in Fig. 3(a). Based on the two statistical measures, sensitivity and specificity, the accuracy of the categorization of the tissues was quantified. Subsequently, the receiver operating characteristic (ROC) curve is also generated as shown in Fig. 3(b) to evaluate the performance of the classification criterion based on the σ of the spatial frequency for distinguishing normal and cancerous brain tissues. The accuracy can be measured using the AUC (area under the ROC curve).

The sensitivity, specificity and the AUC values for SVM classification using the σ of the spatial frequency for brain tissues are summarized in Table 1.

The sensitivity, specificity, accuracy and AUC values in Table 1 demonstrate the excellent efficacy of SVM based on the spatial frequency as a promising diagnostic tool for brain cancer detection.

Table 1. Evaluation of the performance of SVM classification for distinguishing normal and cancerous brain tissues based on σ.

Evaluated components	Sensitivity	Specificity	Accuracy	AUC
Normal versus cancer	88.5%	75.0%	86.7%	0.93

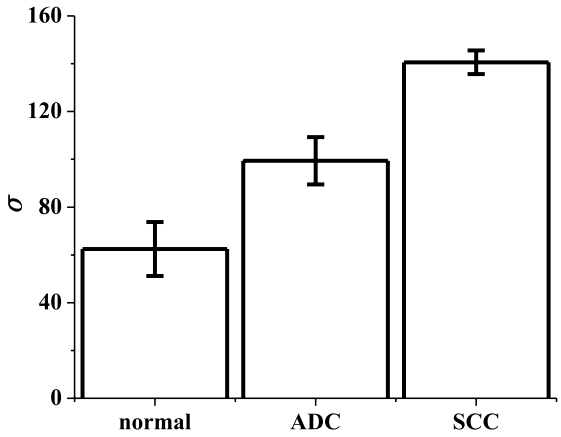

Fig. 4. The increase of σ of the spatial frequency spectra as a function of brain tissue type including normal brain tissue and brain metastases from lung cancers: ADC and SCC.

Figure 4 shows the change in the criterion σ generated by SFSA method from normal to metastatic brain tumor tissues of ADC and SCC. An increase in σ of the spatial frequency is observed from normal to different types of cancerous tissues. This may provide an alternate diagnostic criterion for grading brain tumor tissues. Identifying the primary metastatic potential of cancer is critical in cancer detection and staging. This study is highly relevant to tumor grading by optical techniques and may serve as a key step to predict the primary metastatic potential of brain metastases. It helps in understanding the use of reflectance micrographic images and Raman techniques to identify potential metastatic cancer using intact tissue specimens.

The SFSA–VRR results demonstrated consistency with the histopathology diagnosis (Figs. 1(g)–1(i)). Even though in this study, the classification was performed based on the SFSA of the micrographic images and VRR spectra separately, diagnostic information was observed using the synchronously carried-out SFSA and VRR techniques on the same sites. Therefore, this is a dual-modal technique for cancer diagnosis. A new classifier can be developed that combines the results of SFSA and VRR in future studies for more robust diagnosis.

4. Conclusion

VRR spectra demonstrate an array of biomarkers (e.g., carotenoids, tryptophan, amide II, lipids and proteins) functioning simultaneously in real time

J. Innov. Opt. Health Sci. 2019.12. Downloaded from www.worldscientific.com
by HUAZHONG UNIVERSITY OF SCIENCE AND TECHNOLOGY on 04/14/19. Re-use and distribution is strictly not permitted, except for Open Access articles.

based on which it provides a label-free technique for differentiation of human brain normal tissues from the brain metastases of lung cancers.

An SFSA criterion parameter, σ, as a signature indicator is obtained by SVM based on the width of the Gaussian distribution fitted to the spatial frequency spectra for differentiation of human normal brain tissues from cancerous brain tissues. The SFSA and VRR-combined method can provide the results from simultaneous detections since micrograph images and VRR signals can be measured synchronously.[18,62] More information can be found in Ref. 63. Based on this study, a new optical pathological method based on the dual-modalities of SFSA–VRR may be developed to improve the accuracy of brain biopsy in neuropathology diagnosis and to guide brain surgery.

Conflict of Interest

The authors have no associations with commercial companies that provided support for the work reported in the submitted manuscript or non-financial associations that may be relevant or seen as relevant to the submitted manuscript.

Acknowledgments

This research is supported by The Air Force Medical Center, China and in part of The Institute for Ultrafast Spectroscopy and Lasers (IUSL), the City College of the City University of New York. The authors would like to thank Mr. C. Y. Zhang, Mr. M. Z. Fan and Dr. X. H. Ni for their assistance in the experiments and suggestions concerning this paper.

References

1. "Quick brain tumor facts", National Brain Tumor Society, http://braintumor.org/brain-tumor-information/brain-tumor-facts/.
2. A. Jemal *et al.*, "Cancer statistics, 2004," *CA Cancer J. Clin.* **54**, 8–29 (2004).
3. W. D. Travis, J. Linder, B. Mackay, Classification, histology, cytology, and electron microscopy, *Lung Cancer: Principles and Practice*, H. I. Pass *et al.*, Eds., 2nd Edition, pp. 453–495, Lippincott Williams & Wilkins, Philadelphia (2000).
4. R. F. DeVore III, D. H. Johnson, Chemotherapy for small cell lung cancer, *Lung Cancer: Principles and Practice*, H. I. Pass *et al.*, Eds., 2nd Edition, pp. 923–939. Lippincott Williams & Wilkins, Philadelphia (2000).
5. M. H. T. Reinges, H.-H. Nguyen, T. Krings, B.-O. Hütter, V. Rohde, J. M. Gilsbach, "Course of brain shift during microsurgical resection of supratentorial cerebral lesions: Limits of conventional neuronavigation," *Acta Neurochir. (Wien)* **146**, 369–377 (2004), doi: 10.1007/s00701-003-0204-1.
6. I. J. Gerard, M. Kersten-Oertel, K. Petrecca, D. Sirhan, J. A. Hall, D. L. Collins, "Brain shift in neuronavigation of brain tumors: A review," *Med. Image Anal.* **35**, 403–420 (2017).
7. R. R. Alfano *et al.*, "Laser induced fluorescence spectro scopy from native cancerous and normal tissue," *IEEE J. Quantum Electron.* **20**, 1507–1511 (1984).
8. R. R. Alfano *et al.*, "Human breast tissues studied by IR Fourier transform Raman spectroscopy," *Lasers Life Sci.* **4**, 23–28 (1991).
9. C.-H. Liu *et al.*, "Raman, fluorescence, and time-resolved light scattering as optical diagnostic techniques to separate diseased and normal biomedical media," *J. Photochem. Photobiol. B* **16**(2), 187–209 (1992).
10. Y. Zhou *et al.*, "Human brain cancer studied by resonance Raman spectroscopy," *J. Biomed. Opt.* **17**, 116021 (2012).
11. M. Jermyn, K. Mok, J. Mercier, J. Desroches, J. Pichette, K. Saint-Arnaud, L. Bernstein, M. C. Guiot, K. Petrecca, F. Leblond, "Intraoperative brain cancer detection with Raman spectroscopy in humans," *Sci. Transl. Med.* **7**, 274ra219 (2015).
12. M. Ji *et al.*, "Rapid, label-free detection of brain tumors with stimulated Raman scattering microscopy," *Sci. Transl. Med.* **5**, 201ra119 (2013).
13. A. Imiela, B. Polis, L. Polis, H. Abramczyk, "Novel strategies of Raman imaging for brain tumor research," *Oncotarget* **8**, 85290–85310 (2017).
14. Y. Zhou *et al.*, "Optical pathology of human brain metastasis of lung cancer using combined resonance Raman and spatial frequency spectroscopies," *Proc. SPIE* **9703**, 97031R-1-6 (2016).
15. J. Desroches, M. Jermyn, K. Mok, C. Lemieux-Leduc, J. Mercier, K. St-Arnaud, K. Urmey, M.-C. Guiot, E. Marple, K. Petrecca, F. Leblond, "Characterization of a Raman spectroscopy probe system for intraoperative brain tissue classification," *Biomed. Opt. Express* **6**, 2380–2397 (2015).
16. M. F. Kircher, A. de la Zerda, J. V. Jokerst, C. L. Zavalet, P. J. Kempen, E. Mittr, K. Pitter, R. Huang, C. Campos, F. Habte, R. Sinclair, C. W. Brennan, I. K. Mellinghoff, E. C. Holland, S. S. Gambhir, "A brain tumor molecular imaging strategy using a new triple-modality MRI-photoacoustic-Raman nanoparticle," *Nat. Med.* **18**(5), 829 (2012).

J. Innov. Opt. Health Sci. 2019.12. Downloaded from www.worldscientific.com
by HUAZHONG UNIVERSITY OF SCIENCE AND TECHNOLOGY on 04/14/19. Re-use and distribution is strictly not permitted, except for Open Access articles.

17. C.-H. Liu *et al.*, "Resonance Raman and Raman spectroscopy for breast cancer detection," *Technol. Cancer Res. Treat.* **12**, 371–382 (2013).
18. Y. Zhou *et al.*, "Brain metastasis detection by resonant Raman optical biopsy method," *Proc. SPIE* **8940**, 89400C (2014).
19. C.-H. Liu, B. Wu, L. Sordillo, S. Boydston-White, V. Sriramoju, C. Zhang, H. Beckman, L. Zhang, Z. Pei, L. Shi, R. R. Alfano, "A pilot study for distinguishing basal cell carcinoma from normal human skin tissues using resonance Raman spectroscopy," *J. Cancer Metastasis Treat.* **5**, 4 (2019).
20. Y. Zhou, C.-H. Liu, B. Wu, C. Zhang, X. Yu, G. Cheng, H. Chen, Q. Liang, M. Zhang, K. Zhu, R. R. Alfano, "Invited article: Molecular biomarkers characterization for human brain glioma grading using visible resonance Raman spectroscopy," *APL Photonics* **3**, 120802 (2018).
21. C.-H. Liu *et al.*, "Vulnerable atherosclerotic plaque detection by resonance Raman spectroscopy," *J. Biomed. Opt.* **21**, 127006 (2016).
22. K. Lin, W. Zheng, C. M. Lim, Z. Huang, "Real-time In vivo diagnosis of nasopharyngeal carcinoma using rapid fiber-optic raman spectroscopy," *Theranostics* **7**, 3517–3526 (2017).
23. A. Mizuno, H. Kitajima, K. Kawauchi, S. Muraishi, Y. J. Ozaki, "Near infrared Fourier transform Raman spectroscopic study of human brain tissues and tumours," *J. Raman Spectrosc.* **25**, 25–29 (1994).
24. S. Koljenovic *et al.*, "Discriminating vital tumor from necrotic tissue in human glioblastoma tissue samples by raman spectroscopy," *Lab. Invest.* **82**(10), 1265 (2002).
25. C. Krafft, S. B. Sobottka, G. Schackert, R. Salzer, "Near infrared Raman spectroscopic mapping of native brain tissue and intracranial tumors," *Analyst* **130**, 1070–1077 (2005).
26. R. Pandey, S. K. Paidi, J. W. Kang, N. Spegazzini, Discerning the differential molecular pathology of proliferative middle ear lesions using Raman spectroscopy, *Sci. Rep.* **5**, 13305 (2015).
27. B. Bodanese, L. J. Silveira, R. Albertini, R. A. Zangaro, M. T. T. Pacheco, "Differentiating normal and basal cell carcinoma human skin tissues *in vitro* using dispersive Raman spectroscopy: A comparison between principal components analysis and simplified biochemical models," *Photomed. Laser Surg.* **28**(Suppl 1), S119–S127 (2010).
28. Y. Pu, J. Jagtap, A. Pradhan, R. R. Alfano, "Optical quantitative pathology of cervical intraepithelial neoplasia in human tissues using spatial frequency analysis," *J. Biophotonics* **8**(3), 233–238 (2015).
29. S. Russell, T. A. Nguyen, C. R. Torres, S. Bhagroo, M. J. Russell, R. R. Alfano, "Spatial frequency analysis of high-density lipoprotein and iron-oxide nanoparticle transmission electron microscope image structure for pattern recognition in heterogeneous fields," *J. Biomed. Opt.* **19**(1), 15004 (2014), doi: 10.1117/1.JBO.19.1.015004.
30. Y. Pu, J. Jagtap, A. Pradhan, R. R. Alfano, "Spatial frequency analysis for detecting early stage of cancer in human cervical tissues," *Technol. Cancer Res. Treat.* **13**(5), 421–425 (2014).
31. J. Goodman, *Introduction to Fourier Optics*, 3rd Edition, Roberts & Company, Greenwood Village (2005).
32. SEER ICD-O-3 Coding Materials Archive, Available at http://www.cancer.gov/cancertopics/factsheet/detection/staging/.
33. T. Tanaka, M. Shnimizu, H. Moriwaki, "Cancer chemoprevention by carotenoids," *Molecules* **17**(3), 3202–3242 (2012).
34. I. V. Ermakov, M. Sharifzadeh, M. Ermakov, W. Gellermann, "Resonance Raman detection of carotenoid antioxidants in living human tissue," *J. Biomed. Opt.* **10**, 064028 (2005).
35. M. E. Darvin, W. Sterry, J. Lademann, T. Vergou, "The role of carotenoids in human skin," *Molecules* **16**, 10491 (2011).
36. S. F. Haag *et al.*, "Determination of the antioxidative capacity of the skin *in vivo* using resonance Raman and electron paramagnetic resonance spectroscopy," *Exp. Dermatol.* **20**, 483–487 (2011).
37. J. Lademann, M. C. Meinke, W. Sterry, M. E. Darvin, "Carotenoids in human skin," *Exp. Dermatol.* **20**, 377–382 (2011).
38. M. Wrona, W. Korytowski, M. Rozanowska, T. Sarna, T. G. Truscott, "Cooperation of antioxidants in protection against photosensitized oxidation," *Free Radic. Biol. Med.* **35**, 1319–1329 (2003).
39. P. Palozza, N. I. Krinsky, "Beta-Carotene and alpha-tocopherol are synergistic antioxidants," *Arch. Biochem. Biophys.* **297**, 184–187 (1992).
40. M. E. Darvin, W. Sterry, J. Lademann, "Resonance Raman spectroscopy as an effective tool for the determination of antioxidative stability of cosmetic formulations," *J. Biophotonics* **3**, 82–88 (2010).
41. G. J. Puppels *et al.*, "Development and application of Raman microspectroscopic and Raman imaging techniques for cell biological studies," *J. Mol. Struct.* **347**, 477–484 (1995).
42. G. C. Prendergast, "Why tumours eat tryptophan," *Nature* **478**, 192–194 (2011).
43. P. E. Hanninen, E. Soini, S. W. Hell, "Continuous wave excitation two-photon fluorescence microscopy," *J. Microsc.* **176**, 222–225 (1994).
44. S. T. Mayne *et al.*, "Resonance Raman spectroscopic evaluation of skin carotenoids as a biomarker of

J. Innov. Opt. Health Sci. 2019.12. Downloaded from www.worldscientific.com
by HUAZHONG UNIVERSITY OF SCIENCE AND TECHNOLOGY on 04/14/19. Re-use and distribution is strictly not permitted, except for Open Access articles.

carotenoid status for human studies," *Arch. Biochem. Biophys.* **539**(1), 1–18 (2013).
45. I. V. Ermakov *et al.*, "Skin carotenoids as biomarker for vegetable and fruit intake: Validation of the reflection-spectroscopy based "Veggie Meter"," *FASEB J.* **30**(1_supplement), 409.3 (2016).
46. H. Ren, J. D. Biggs, S. Mukamel, "Two-dimensional stimulated ultraviolet resonance Raman spectra of tyrosine and tryptophan: A simulation study," *J. Raman Spectrosc.* **44**, 544–559 (2013).
47. E. B. J. Wilson, "The normal modes and frequencies of vibration of the regular plane hexagon model of the benzene molecule," *Phys. Rev.* **45**, 706 (1934).
48. R. P. Rava, T. G. Spiro, "Resonance enhancement in the ultraviolet Raman spectra of aromatic amino acids," *J. Phys. Chem.* **89**, 1856–1861 (1985).
49. R. P. Rava, T. G. Spiro, "Selective enhancement of tyrosine and tryptophan resonance Raman spectra via ultraviolet laser excitation," *J. Am. Chem. Soc.* **106**, 4062–4064 (1984).
50. C. A. Opitz *et al.*, "An endogenous tumour-promoting ligand of the human aryl hydrocarbon receptor," *Nature* **478**, 197–203 (2011).
51. F. Moroni, "Tryptophan metabolism and brain function: Focus on kynurenine and other indole metabolites," *Eur. J. Pharmacol.* **375**, 87–100 (1999).
52. E. W. Yue *et al.*, "INCB24360 (Epacadostat), a highly potent and selective indoleamine-2,3-dioxygenase 1 (IDO1) inhibitor for Immuno-oncology," *ACS Med. Chem. Lett.* **8**, 486–491 (2017).
53. R. Campanella, "Membrane lipids modifications in human gliomas of different degree of malignancy," *J. Neurosurg. Sci.* **36**, 11–25 (1992).
54. P. P. Sordillo, L. A. Sordillol, L. Helson, "The kynurenine pathway: A primary resistance mechanism in patients with glioblastoma," *Anticancer Res.* **37**, 2159–2171 (2017), doi: 10.21873/anticanres.11551.
55. B. Hoffman *et al.*, *Williams Gynecology*, 2nd Edition, McGraw-Hill Professional, New York (2012).
56. D. F. Gleason, G. T. Mellinger, "Prediction of prognosis for prostatic adenocarcinoma by combined histological grading and clinical staging," *J. Urol.* **111**, 58–64 (1974).
57. H. J. G. Bloom, W. W. Richardson, "Histological grading and prognosis in breast cancer: A study of 1409 cases of which 359 have been followed for 15 years," *Br. J. Cancer* **11**(3), 359–377 (1957).
58. N. Efford, *Digital Image Processing: A Practical Introduction Using Java*™, Pearson Education, Addison-Wesley, Harlow, England (2000).
59. C. Cortes, V. N. Vapnik, "Support-vector networks," *Mach. Learn.* **20**, 273–297 (1995).
60. Y. Sun, Y. Pu, Y. Yang, R. R. Alfano, "Biomarkers spectral subspace for cancer detection," *J. Biomed. Opt.* **17**(10), 107005-1–107005-9 (2012).
61. X. Y. Xu, Z. Z. Liu, Q. F. Wu, "A novel K-nearest neighbor classification algorithm based on maximum entropy," *Int. J. Adv. Comput. Technol.* **5**(5), (2013).
62. Y. Zhou *et al.*, "Resonance Raman Spectroscopy of human brain metastasis of lung cancer analyzed by blind source separation," *Proc. SPIE* **10051**, 100511I-1-7 (2017).
63. Y. Zhou, C.-H. Liu, K. Zhu, B. Wu, X. Yu, R. R. Alfano, "Visible resonance Raman spectroscopy in human brain tissues," *Neurophotonics and Biomedical Spectroscopy*, R. R. Alfano, L. Shi, Eds., pp. 65–106, Elsevier, Amsterdam, Netherlands (2018).